Ultrasound in Med. & Biol., Vol. 44, No. 7, pp. 1504–1515, 2018

0301-5629/$ - see front matter

https://doi.org/10.1016/j.ultrasmedbio.2018.03.014

● *Original Contribution*

ANALYSIS OF TRANSIENT SHEAR WAVE IN LOSSY MEDIA

KEVIN J. PARKER,* JUVENAL ORMACHEA,* SCOTT WILL,† and ZAEGYOO HAH‡

* Department of Electrical and Computer Engineering, University of Rochester, Rochester, New York, USA; † Institute of Optics, University of Rochester, Rochester, New York, USA; and ‡ Samsung Medison Company, Ltd., Seoul, South Korea

(*Received* 14 *November* 2017; *revised* 15 *March* 2018; *in final form* 16 *March* 2018)

Abstract—The propagation of shear waves from impulsive forces is an important topic in elastography. Observations of shear wave propagation can be obtained with numerous clinical imaging systems. Parameter estimations of the shear wave speed in tissues, and more generally the viscoelastic parameters of tissues, are based on some underlying models of shear wave propagation. The models typically include specific choices of the spatial and temporal shape of the impulsive force and the elastic or viscoelastic properties of the medium. In this work, we extend the analytical treatment of 2-D shear wave propagation in a biomaterial. The approach applies integral theorems relevant to the solution of the generalized Helmholtz equation, and does not depend on a specific rheological model of the tissue's viscoelastic properties. Estimators of attenuation and shear wave speed are derived from the analytical solutions, and these are applied to an elastic phantom, a viscoelastic phantom and *in vivo* liver using a clinical ultrasound scanner. In these samples, estimated shear wave group velocities ranged from 1.7 m/s in the liver to 2.5 m/s in the viscoelastic phantom, and these are lower-bounded by independent measurements of phase velocity. (E-mail: kevin.parker@rochester.edu)

Key Words: **Ultrasound, Elastography, Shear waves, Group velocity, Viscoelastic tissue.**

INTRODUCTION

A number of techniques have been developed to estimate and image the elastic properties of tissues (Doyley 2012; Parker et al. 2011). These provide useful biomechanical and clinically relevant information not available from conventional radiology. A subset of techniques utilize acoustic radiation force from short-duration pushing pulses as an initial condition, which then results in a propagating shear wave. Through tracking of the propagating wave, the shear wave velocity can be estimated, and this yields the Young's modulus—or stiffness—of the material (Sarvazyan et al. 1998). A variety of approaches employing radiation force, with important clinical applications, have been developed (Fatemi and Greenleaf 1998; Hah et al. 2012; Hazard et al. 2012; Konofagou and Hynynen 2003; McAleavey and Menon 2007; Nightingale et al. 1999; Parker et al. 2011).

In lossy tissues, however, a propagating shear wave produced by a focused ultrasound beam's radiation force will rapidly diminish within a few millimeters from the source. Furthermore, the displacement wave has an extended "tail," and its original shape becomes distorted. These effects complicate attempts to track the key features of the propagating pulse to estimate shear wave speed. Analytical and numerical models have been proposed to model the evolution and decay of pulses in viscoelastic media (Bercoff et al. 2004a; Fahey et al. 2005; Kazemirad et al. 2016; Leartprapun et al. 2017; Nenadic et al. 2017; Nightingale et al. 1999; Parker and Baddour 2014; Sarvazyan et al. 1998; Schmitt et al. 2010; Vappou et al. 2009; Wijesinghe et al. 2015). However, there is still the need for a closed-form analytical solution that clearly identifies the key terms responsible for the distortion and decay of the pulse. Furthermore, there are different models for wave propagation in lossy media (Bercoff et al. 2004b; Chen et al. 2004; Chen and Holm 2003; Giannoula and Cobbold 2008, 2009; Szabo 1994; Urban et al. 2009). Because there is no consensus yet as to the most appropriate model and mechanism of loss for shear waves in soft tissues, it is useful to have analytical expressions that are independent of any particular model, but still valid over the operating range of shear wave frequencies.

The approach taken in this article follows the earlier framework of Parker and Baddour (2014). First, the governing equations and transforms are stated in a progression

Address correspondence to: Kevin J. Parker, University of Rochester, Hopeman Engineering Building 203, PO Box 270126, Rochester, NY 14627-0126, USA. E-mail: kevin.parker@rochester.edu

favored by the classic treatment of Graff (1975). Then, a 2-D beam pattern is introduced, and the equations are reduced to simplified forms. General viscoelastic material properties are simplified to first-order (Taylor series expansion) terms and introduced into the analytic solutions, retaining leading terms. From these, some estimators of tissue parameters can be specified. Some preliminary examples are then presented, in which the data are taken from a clinical imaging scanner.

THEORY

We model the applied radiation force as being long and relatively constant in the z (depth) direction, so that spatial derivatives in the z direction are small compared with other terms. In practice, this is commensurate with a higher f-number focus in a weakly attenuating medium and multidepth push sequences. In this case, we assume that the following holds for displacements u and body forces f:

$$\begin{aligned} u_x &= u_y = 0, \quad u_z = u_z(x, y, t) \\ f_x &= f_y = 0, \quad f_z = f_z(x, y, t) \end{aligned} \tag{1}$$

In these circumstances, the governing equations for displacements in the medium reduce to

$$\mu \nabla^2 u_z + \rho f_z = \rho \ddot{u}_z, \quad \nabla^2 = \frac{\partial^2}{\partial x^2} + \frac{\partial^2}{\partial y^2} \tag{2}$$

where μ is the shear modulus and ρ is the density of the medium. The particle motions are polarized in a single direction z, and the resulting waves will be shear waves propagating at the velocity $c = \sqrt{\mu/\rho}$ (Graff 1975).

By taking the spatial and temporal Fourier transform of the governing equation, and then the inverse transform, we find the solution is given by

$$u_z(x, y, t) = \frac{1}{(2\pi)^{3/2}} \iiint \frac{F(\varepsilon, \eta, \omega)}{\varepsilon^2 + \eta^2 - (\omega^2/c^2)} \mathbf{e}^{i(\varepsilon x + \eta y - \omega t)} d\varepsilon d\eta d\omega \tag{3}$$

where $F(\varepsilon, \eta, \omega)$ is the Fourier transform of $c^2 f(x, y, t)$, the applied radiation force pulse. Assuming $f(x, y, t)$ is a sufficiently short pulse so as to be modeled as an impulse in time (Zvietcovich et al. 2017) and Gaussian in (x, y) with spatial width of (σ_x, σ_y), respectively,

$$F(\varepsilon, \eta, \omega) = 1\mathbf{e}^{-\frac{1}{2}\left(\sigma_x^2 \varepsilon^2 + \sigma_y^2 \eta^2\right)} \tag{4}$$

Substituting the particular form yields

$$u_z(x, y, t) = \frac{1}{(2\pi)^{3/2}} \iiint \frac{\mathbf{e}^{-\frac{1}{2}\left(\sigma_x^2 \varepsilon^2 + \sigma_y^2 \eta^2\right)}}{\varepsilon^2 + \eta^2 - (\omega^2/c^2)} \mathbf{e}^{i(\varepsilon x + \eta y - \omega t)} d\varepsilon d\eta d\omega \tag{5}$$

The direct solution of eqn (5) involves treatment of the singularity formed by the denominator becoming zero when $\varepsilon^2 + \eta^2 = \omega^2/c^2 = k^2$. Baddour (2011) has insightfully explained how the denominator serves as a "sifting" property, meaning the solution is completely governed by the integrand evaluated at the singularity. For example, Baddour's theorem 5 for complex exponentials and a real wave number is

$$I(k, r) = \int_{-\infty}^{\infty} \frac{\phi(\eta)}{\eta^2 - k_t^2} \mathbf{e}^{i\eta r} d\eta = \frac{i \cdot \pi}{k_t} \phi(k_t) \mathbf{e}^{ik_t r} \quad r > 0 \tag{6}$$

Effectively, this transforms the spatial transform $\phi(\eta)$ related to the distribution of force and converts it to a temporal transform $\phi(k)$, where the singularity caused by the denominator selects the value of k. Thus, considering the integration of eqn (5) over the spatial frequencies, we examine the quantity

$$\phi(k) = \iint \left(\mathbf{e}^{-\frac{1}{2}\left(\sigma_x^2 \varepsilon^2 + \sigma_y^2 \eta^2\right)} \right) \left(\mathbf{e}^{i(\varepsilon x + \eta y)} \right) d\varepsilon dn \tag{7}$$

on the circle defined by $\varepsilon^2 + \eta^2 = k^2$. Substituting $\varepsilon = k \cos \theta$, $\eta = k \sin \theta$, $d\varepsilon dn = r dr d\theta = |k| dr d\theta$, considering first the integration over r, and comparing with eqn (6) from Baddour's theorem 5, we have

$$u_z(x, y, k) = \frac{-i \operatorname{sign}(k)}{8\pi} \int_0^{2\pi} \mathbf{e}^{-\frac{k^2}{2}\left(\sigma_x^2 (\cos\theta)^2 + \sigma_y^2 (\sin\theta)^2\right)} \mathbf{e}^{ik(x\cos\theta + y\sin\theta)} d\theta \tag{8}$$

Rewriting the $\mathbf{e}^{-\frac{k^2}{2}(\ )}$ term for the case where $\sigma_y > \sigma_x$ (as is common in 1-D linear arrays, where y represents the elevational direction),

$$= \mathbf{e}^{-\frac{k^2 \sigma_x^2}{2}\left(\cos^2\theta + R^2 \sin^2\theta\right)} \tag{9}$$

where $R^2 = \sigma_y^2/\sigma_x^2$, and could be 4 to 100 depending on the particular array.

No closed-form analytical solution to eqn (8) has been found. However, for the special case of radial symmetry, where $R = 1$, and on the x-axis, where $y = 0$, eqn (8) reduces to

$$u_{zs}(x,0,k)=\frac{-i\mathrm{sign}(k)}{8\pi}\int_0^{2\pi}\mathbf{e}^{-\frac{k^2\sigma_x^2}{2}}\mathbf{e}^{ikx\cos\theta}d\theta$$
$$=\frac{-i\mathrm{sign}(k)}{8}\mathbf{e}^{-\frac{k^2\sigma_x^2}{2}}J_0(kx) \quad (10)$$

Substituting $k=\omega/c$ and applying causality to the temporal Fourier transform (see Parker and Baddour 2014, eqn 23), we find

$$u_{zs}(x,0,t)=\int_0^{\infty}\mathbf{e}^{-\left(\frac{\omega}{c}\right)^2\frac{\sigma_x^2}{2}}J_0\left(\omega\cdot\frac{x}{c}\right)\sin(\omega t)d\omega \quad (11)$$

which is similar to the result in Parker and Baddour (2014, eqn 29) for a radial symmetric beam derived in cylindrical coordinates using Hankel transforms.

For large values of R produced by 1-D arrays, the magnitude of eqn (9) falls off rapidly with θ, and most of the energy in the integral of eqn (8) is therefore concentrated near $\theta=0$. Thus, we can apply the small-angle approximation: $\cos\theta\cong 1-\theta^2$, $\cos^2\theta\cong 1$, and $R^2\sin^2\theta\cong R^2\theta^2$. Then, eqn (8) evaluated along the y-centerline $(x, y=0)$ becomes

$$u_z(x,0,k)=\frac{-isign(k)}{8\pi}\int_0^{2\pi}\mathbf{e}^{-\frac{1}{2}k^2\sigma_x^2\left(1+R^2\theta^2\right)}\mathbf{e}^{ikx\left(1-\theta^2\right)}d\theta \quad (12)$$

$$u_z(x,0,k)=A_1 isign(k)\mathbf{e}^{-\frac{1}{2}k^2\sigma_x^2}\frac{\mathrm{Erf}\left[\sqrt{2\pi}\sqrt{k^2\sigma_y^2+2ikx}\right]}{\sqrt{k^2\sigma_y^2+2ikx}}\mathbf{e}^{ikx} \quad (13)$$

where A_1 accumulates all constants. The velocity can be written as

$$v_z(x,0,k)=-i\omega u_z\left(x,0,\frac{\omega}{c}\right) \quad (14)$$

Finally, we obtain $u_z(x,0,t)$ as the inverse Fourier transform of eqns (13) and (14), and by the properties of the Fourier transform we can write the inverse as a convolution of functions for cases of small x, assuming we can ignore the imaginary part of the square roots in eqn (13) where $x\ll k\sigma_y^2$. Then,

$$u_z(x,0,t)\cong\left(\frac{A_1}{t}\right)*\left(\Gamma\left[0,\frac{(ct)^2}{(\pi\sigma_y)^2}\right]\right)*\left(\mathbf{e}^{\left[\left(\frac{-c^2}{4\sigma_x^2}\right)\left(t-\frac{x}{c}\right)^2\right]}\right) \quad (15)$$

The third term is a Gaussian function shaped by the x-axis beamwidth σ_x and delayed in time by propagation to the observation point $(x,0)$. But this is convolved with the first term, essentially a Hilbert transform operation producing a Dawson function (Abramowitz and Stegun 1964; Poularikas 2010), and is also convolved with a gamma function (second term), which serves as a type of low-pass filter with long tails. The net result is the observed displacement wave in an elastic, lossless medium.

The approximate magnitude and phase dependence of $u_z(x,0,k)$ will become important in the next section, where parameter estimation is examined. By use of geometric interpretations of the arguments of eqn (13), when $x>\sigma_x>0$, $\omega>0$ and $R>1$, and for points $x_1>x_0$, the following approximations can be made:

$$|u_z(x_1,0,\omega)|\approx|u_z(x_0,0,\omega)|\left(\sqrt{\frac{\pi x_0+\left(\frac{\omega}{c}\right)\sigma_y^2}{\pi x_1+\left(\frac{\omega}{c}\right)\sigma_y^2}}\right) \quad (16)$$

and

$$\measuredangle u_z(x_1,0,\omega)\approx\frac{1}{2}\left[\left(\frac{\omega}{c}x_1\right)+\left(\frac{\omega}{c}\sqrt{x_1^2+\sigma_y^2}\right)-\left(\frac{\pi}{2}\right)\right] \quad (17)$$

These approximate relations can be useful in deriving simplified estimators for the parameters if the desire is to simplify the magnitude and phase of eqns (13) and (14). However, as Figure 1(b) illustrates, the issue of phase unwrapping or modulo 2π operations is present in phase operations. These are altered by dispersion, which is considered next.

For the general treatment of a lossy material, we introduce first-order dispersion terms as a Taylor series approximation over a limited bandwidth, so that k is complex, $k=(\omega/c)-i\alpha$, and to first order, $c\equiv c_0+c_1|\omega|$; $\alpha=\alpha_0+\alpha_1|\omega|$ where $c_0\gg c_1\omega$. However, for low-pass functions like the Gaussian, the behavior of c and k near zero frequency is particularly important. Under most conventional loss mechanisms (Blackstock 2000:ch. 9), as $\omega\to 0$, $c\to c_0$ and $\alpha\to 0$. Thus $\alpha_0=0$ for low-pass functions in conventional lossy media. Substituting these into eqn (13) and again assuming weak attenuation, $\alpha\ll(\omega/c)$; then, retaining only the most significant terms, we find

$$u_d(x,\omega)=u_z(x,0,\omega)\cdot\mathbf{e}^{-x|\omega|\alpha_1}\cdot\mathbf{e}^{-ix\left(\frac{\omega}{c_0}-\frac{c_1\omega^2\mathrm{sign}[\omega]}{c_0^2}\right)} \quad (18)$$

where a first-order series expansion

$$\frac{1}{1+\frac{c_1}{c_0}|\omega|}\cong 1-\frac{c_1}{c_0}|\omega|$$

is used in the phase term, and $u_z(x,0,\omega)$ is given by eqn (13).

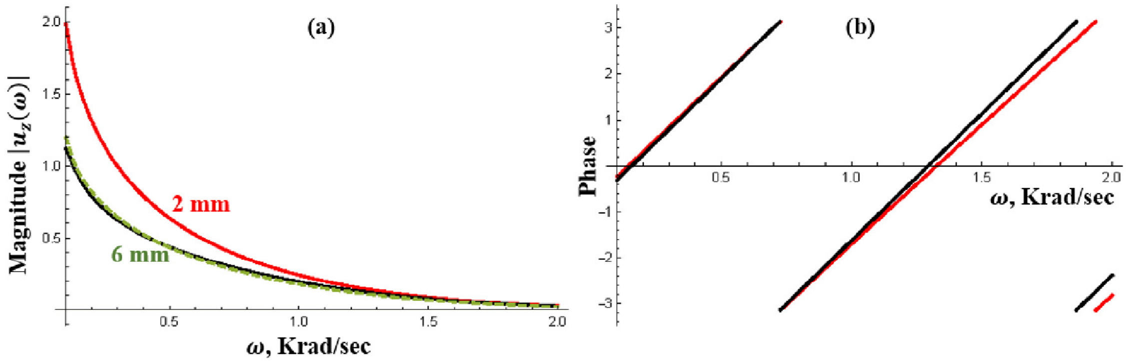

Fig. 1. (a) Magnitude of the Fourier transform of the shear wave displacement as a function of frequency measured at 2 mm from the central beam axis (*upper curve*) and at 6 mm (*lower curve*). The *dashed curve* is the approximate correction factor, eqn (16), that accounts for geometric spreading as a function of frequency and distance, applied to the 2-mm curve. Once corrected for geometric spreading, the effects of attenuation can be more accurately measured. Other parameters used in this example: $\sigma_x = 1$ mm, $R = 3$, $c = 1$ m/s. (b) Phase of the Fourier transform of the shear wave displacement as a function of frequency measured 5 mm from the central beam axis. The *red curve* is the exact phase from eqn (13), whereas the *black curve* is the approximate relation given in eqn (17), but calculated modulo 2π. Other parameters used in this example: $\sigma_x = 1$ mm and $\sigma_y = 3$ mm.

Now, examining the magnitude and phase of the temporal transform,

$$|u_d(x,\omega)| = |u_z(x,0,\omega)|\left(\mathbf{e}^{-(\alpha_1|\omega|x)}\right) \tag{19}$$

and $\measuredangle u_d(x,\omega) = [\omega/(c_0 + c_1|\omega|)]x$. Thus, given two temporal Fourier transformed waveforms $u_d(x_0,\omega)$ and $u_d(x_1,\omega)$, where $x_1 > x_0$ and $x_1 - x_0 \equiv \Delta x_1$,

$$\measuredangle u_d(x_1,\omega) = \left(\frac{\omega}{c_0 + c_1|\omega|}\right)\left[\frac{1}{2}\left(x_1 + \sqrt{x_1^2 + \sigma_y^2}\right) + \phi\right] \tag{20}$$

and

$$\frac{|u_d(x_1,\omega)|}{|u_d(x_0,\omega)|} = \left(\mathbf{e}^{-\alpha_1|\omega|\Delta x_1}\right)\left(\sqrt{\frac{\pi x_0 + \left(\frac{\omega}{c}\right)\sigma_y^2}{\pi x_1 + \left(\frac{\omega}{c}\right)\sigma_y^2}}\right) \tag{21}$$

We can use eqn (21) to remove the effects of geometric spreading, which are captured by the rightmost terms in that equation. Specifically, for each x_1, we define the corrected waveform $u'_d(x_1,\omega)$ by

$$u'_d(x_1,\omega) \equiv u_d(x_1,\omega)\sqrt{\frac{\pi x_1 + \left(\frac{\omega}{c}\right)\sigma_y^2}{\pi x_0 + \left(\frac{\omega}{c}\right)\sigma_y^2}} \tag{22}$$

The ratio of the magnitudes of the corrected waveforms $u'_d(x_1,\omega)$ to the reference waveforms $u_d(x_0,\omega)$ is then given by

$$\left|\frac{u'_d(x_1,\omega)}{u_d(x_0,\omega)}\right| = \mathbf{e}^{-\alpha_1|\omega|\Delta x} \tag{23}$$

Taking the natural logarithm of eqn (23), we obtain

$$-\left(\ln\left|u'_d(x_1,\omega)\right| - \ln\left|u_d(x_0,\omega)\right|\right) = \alpha_1\omega\Delta x \tag{24}$$

We now proceed by adopting matrix-vector notation. Define the vectors

$$\Delta\boldsymbol{x} \equiv \left[\Delta x_1 \cdots \Delta x_m \cdots \Delta x_M\right]^T \in \mathbb{R}^M \tag{25}$$

where $\Delta x_j = (x_j - x_0)\,\forall j = \{1 \ldots M\}$ and

$$\boldsymbol{\omega} \equiv \left[\omega_1 \cdots \omega_n \cdots \omega_N\right]^T \in \mathbb{R}^N \tag{26}$$

representing the transverse coordinates of the pixels in the field of view (excluding the reference coordinate x_0) and the vector of signal frequencies, respectively. Also, define the matrix $\mathbb{U}_\alpha$ with

$$U_{mn} \equiv -\left(\ln\left|u'_d(x_1,\omega)\right| - \ln\left|u_d(x_0,\omega)\right|\right) \tag{27}$$

The problem of estimating α_1 can then be written as an estimation problem of the form

$$\mathbb{U}_\alpha = \alpha_1\Delta\mathbf{x}\boldsymbol{\omega}^T \tag{28}$$

We can derive a least-squares estimator for α_1 (see Appendix A) of the form

$$\alpha = \frac{\Delta\mathbf{x}^T\mathbb{U}_\alpha\boldsymbol{\omega}}{\left(\Delta\mathbf{x}^T\Delta\mathbf{x}\right)\left(\boldsymbol{\omega}^T\boldsymbol{\omega}\right)} \tag{29}$$

It is important to note that the preceding estimation problem is a special case of the more general problem of fitting a bivariate surface of the form

$$S(x,\omega)=a_0+a_1x+a_2\omega+a_3x\omega+a_4x^2+a_5\omega^2 \quad (30)$$

where $a_3=\alpha_1$. Although our signal model strongly suggests that all $a_j=0$ for $j\neq 3$, it may nevertheless be advantageous in certain circumstances to estimate α using a surface of the form of $S(x,y)$; this approach is considered in Appendix B. Specifically, we note that the least-squares estimator obtained by solving the unconstrained least-squares estimation problem and allowing all a_k to freely vary will yield an unbiased estimator for α (*i.e.,* residuals are zero mean), whereas constraining one or more parameters to equal zero will yield a biased estimator.

Estimating shear wave speed c_0

We proceed in a manner similar to that of the derivation above for the attenuation coefficient α_1.

Given eqn (20), we can then write the displacement wave in the form

$$u_d(x,\omega)=|u_d(x,\omega)|\exp\left\{-i\left(\frac{\omega}{c_0+c_1|\omega|}\right)\left[\frac{1}{2}\left(x+\sqrt{x^2+\sigma_y^2}\right)+\phi\right]\right\} \quad (31)$$

Taking the complex argument $\arg\{\cdot\}$ of both sides and neglecting second-order dispersion, we obtain

$$-\arg\{u_d(x,\omega)\}=\frac{\omega}{c_0}\left[\frac{1}{2}\left(x+\sqrt{x^2+\sigma_y^2}\right)+\phi\right] \quad (32)$$

Next, we can redefine the phase reference point to eliminate ϕ and additionally define a new transverse coordinate $x'\equiv x+\sqrt{x^2+\sigma_y^2}$ to obtain the expression

$$-\arg\{u_d(x,\omega)\}=\frac{1}{2c_0}\omega x' \quad (33)$$

We may now formulate eqn (33) as a least-squares estimation problem by defining the vectors

$$\mathbf{x}'\equiv[x_1'\ldots x_m'\ldots x_M']^T\in\mathbb{R}^M \quad (34)$$

and

$$\boldsymbol{\omega}\equiv[\omega_1\ldots\omega_n\ldots\omega_N]^T\in\mathbb{R}^N \quad (35)$$

and this time defining a new system matrix $\mathbb{U}_c$ according to the prescription

$$U_{mn}=-2\left(\arg\{u_d(x,\omega)\}\right) \quad (36)$$

so that the estimation problem can be written in the form

$$\mathbb{U}_c=\frac{1}{c_0}\mathbf{x}'\boldsymbol{\omega}^T \quad (37)$$

which has a least-squares solution given by

$$\frac{1}{c_0}=\frac{\boldsymbol{x}^T\mathbb{U}_c\boldsymbol{\omega}}{(\boldsymbol{x}^T\boldsymbol{x})(\boldsymbol{\omega}^T\boldsymbol{\omega})}\Rightarrow c_0=\frac{(\boldsymbol{x}^T\boldsymbol{x})(\boldsymbol{\omega}^T\boldsymbol{\omega})}{\boldsymbol{x}^T\mathbb{U}_c\boldsymbol{\omega}} \quad (38)$$

As before, we may also wish to produce an unbiased estimator of c_0 by solving an unconstrained problem of polynomial form of eqn (30), in which case we can recover the shear wave speed c_0 via

$$a_3=\frac{1}{c_0} \quad (39)$$

However, to eliminate all phase unwrapping issues, we next propose an alternative time domain estimate.

Kinetic energy estimators for group velocity

By definition, the kinetic energy of a wave is proportional to $(1/2)\rho V^2$ (where ρ is the density of the medium and V is the local velocity), and in wave motion the total energy is proportional to the kinetic plus the stored energy, and both forms are proportional to V^2 (Blackstock 2000:ch. 1). From eqns (12) to (18) we find that the temporal transform of the velocity wave is

$$v_z(x,0,\omega)=-A_1\omega\cdot\operatorname{sign}(\omega)\cdot\mathbf{e}^{-\frac{1}{2}\left(\frac{\omega}{c}\right)^2\sigma_x^2}\cdot\mathbf{e}^{-\alpha|\omega|x}\cdot\operatorname{Erf}\frac{\left[2\pi\sqrt{\left(\frac{\omega}{c}\right)^2\sigma_y^2+2i\omega\left(\frac{x}{c}\right)}\right]}{\sqrt{\left(\frac{\omega}{c}\right)^2\sigma_y^2+2i\omega\left(\frac{x}{c}\right)}}\cdot\mathbf{e}^{i\omega\left(\frac{x}{c}\right)} \quad (40)$$

and invoking causality,

$$v_z(x,t)=\int_0^\infty\operatorname{Re}[v_z(x,0,\omega)]\cos(\omega t)\,d\omega \quad (41)$$

Defining $k(x,t)=[v_z(x,t)]^2$, the total kinetic energy $K(x)$, by Parseval's theorem, is given by

$$K(x)=\int_0^\infty[v_z(x,t)]^2\,dt=\int_0^\infty\operatorname{Re}[v_z(x,0,\omega)]^2\,d\omega \quad (42)$$

The first moment of $k(x,t)$ can be used to determine c, because the kinetic energy travels with the wave (Biot 1957; Blackstock 2000:ch. 1; Broer 1951). From Bracewell (1996), the centroid $\overline{t_x}$ can be found as

$$\overline{t}_x = \int_0^\infty t \cdot k(x,t)\,dt \Big/ \int_0^\infty k(x,t)\,dt \qquad (43)$$

The linear fit of $\overline{t}_x$ versus x yields the group velocity. Then numerical integration of eqn (42), where all parameters are known except for α, can produce a family of curves which are compared to the measured $K(x)$ to determine the mean squared error estimate of α.

METHODS

A Samsung ultrasound system (Model RS85, Samsung Medison, Seoul, South Korea) and a curved array ultrasound transducer (Model CAI_7A, Samsung Medison) were used to produce push beams and track the induced displacements. In this experiment, fewer than 100 central elements of the transducer were used to transmit focused push beams (center frequency = 2.5 MHz, 130-μs push duration, multifocal depth operation with four sequential pushes along an axial line at regular spacings over 30 mm of increasing focal depth). For a 60-mm focus, the *f*-number is approximately 1.3. The sampling frame rate was 7.5 kHz. After push transmission, the Samsung system immediately switched to plane wave imaging mode using 135 transducer elements (center frequency = 2.5 MHz). The sampling frequency was set to 20 MHz. Some averaging over depth and noise reduction filtering are applied to the displacement estimates; the precise details are proprietary to Samsung.

RESULTS

CIRS breast phantom

Shear waves were produced in the CIRS breast phantom (Model 059, Computerized Imaging Reference Systems, Norfolk, VA, USA). The Samsung RS85 system was used to produce a 2.5-MHz push beam. Measured pulses are illustrated in Figure 2(a) at 0.65 ms and in Figure 2(b) as a function of time for four different lateral observation points. Although the breast phantom is almost a purely elastic medium with low viscosity and attenuation, the pulse shape displays a reduction in amplitude with distance, principally because of the geometric spreading. In Figure 2(c) are the theoretical shapes, taken from numerical integration of the inverse Fourier transform of eqns (13) and (14) and with parameters $c = 2.12$ m/s, $\sigma_x = 1.3$ mm, $R = 2$ and $\alpha = 0.067$ Np/mm/kHz. The value for c was taken from the kinetic energy moments estimate, and the values of σ and R were taken from measurements of the push-pulse beamplots at the selected depth. The attenuation parameter α was determined to be in the range 0.69 ± 0.015 Np/mm/kHz by our constrained least-squares method, and the lower value was used in the model to produce Figure 2(c). The support in the temporal frequency domain for this estimator is illustrated in Figure 3(a).

CIRS viscoelastic phantom

Shear waves were produced in a custom-made CIRS viscoelastic phantom (Serial No. 2095.1-1, Computerized Imaging Reference Systems). Similar to the previous case, a 2.5-MHz push beam was used. Measured pulses are illustrated in Figure 4(a) at 0.65 ms and in Figure 4(b) as a function of time for four different lateral observation points. In a viscoelastic medium, the pulse shape exhibits higher loss than the breast phantom because of the geometric spreading, attenuation and higher viscosity. In Figure 4(c) are the theoretical shapes taken from numerical integration of the inverse Fourier transform of eqns (13) and (14) with parameters $c = 2.46$ m/s, $\sigma_x = 1.3$ mm, $R = 8$, and $\alpha = 0.667$ Np/mm/kHz. The value for c was taken from the kinetic energy moments estimate, whereas the values of σ and R were taken from measurements of the focal beamplots at the selected depth. The attenuation parameter α was determined to be in the range 0.606 ± 0.063 Np/mm/kHz by our constrained least-squares method, and the lower value was used in the model to produce Figure 2(c). The support in the temporal frequency domain for this estimator is illustrated in Figure 3(b).

In vivo human liver

The Samsung system was also used to obtain shear waves in a normal volunteer, under the requirements of informed consent and the University of Rochester institutional review board. A snapshot of the 2-D measured tissue velocity at 0.65 ms following the initiation of the push sequence is provided in Figure 5(a). Measured velocity waveforms at four locations are provided in Figure 5(b), and their spectra in Figure 3(c). Using the forward propagation model and parameters obtained from the estimators $c = 1.74$ m/s, $\sigma_x = 1.3$ mm, $R = 8$ and $\alpha = 1.28$ Np/mm/kHz yields the predicted waveforms illustrated in Figure 5(c). The value for c was taken from the kinetic energy moments estimate, and the values of σ and R were taken from measurements of the focal beamplots. The attenuation parameter α was determined to be 1.15 ± 0.14 Np/mm/kHz by our constrained least-squares method.

DISCUSSION

From Figures 2, 4 and 5, we find a close correspondence of the forward model predictions of shear wave velocity waveforms with the measured waveforms. The forward model incorporates all the assumptions and approximations mentioned in the derivations from eqns (10) to (23) and utilizes the estimated parameters c (kinetic energy group velocity) and α (constrained least-squares

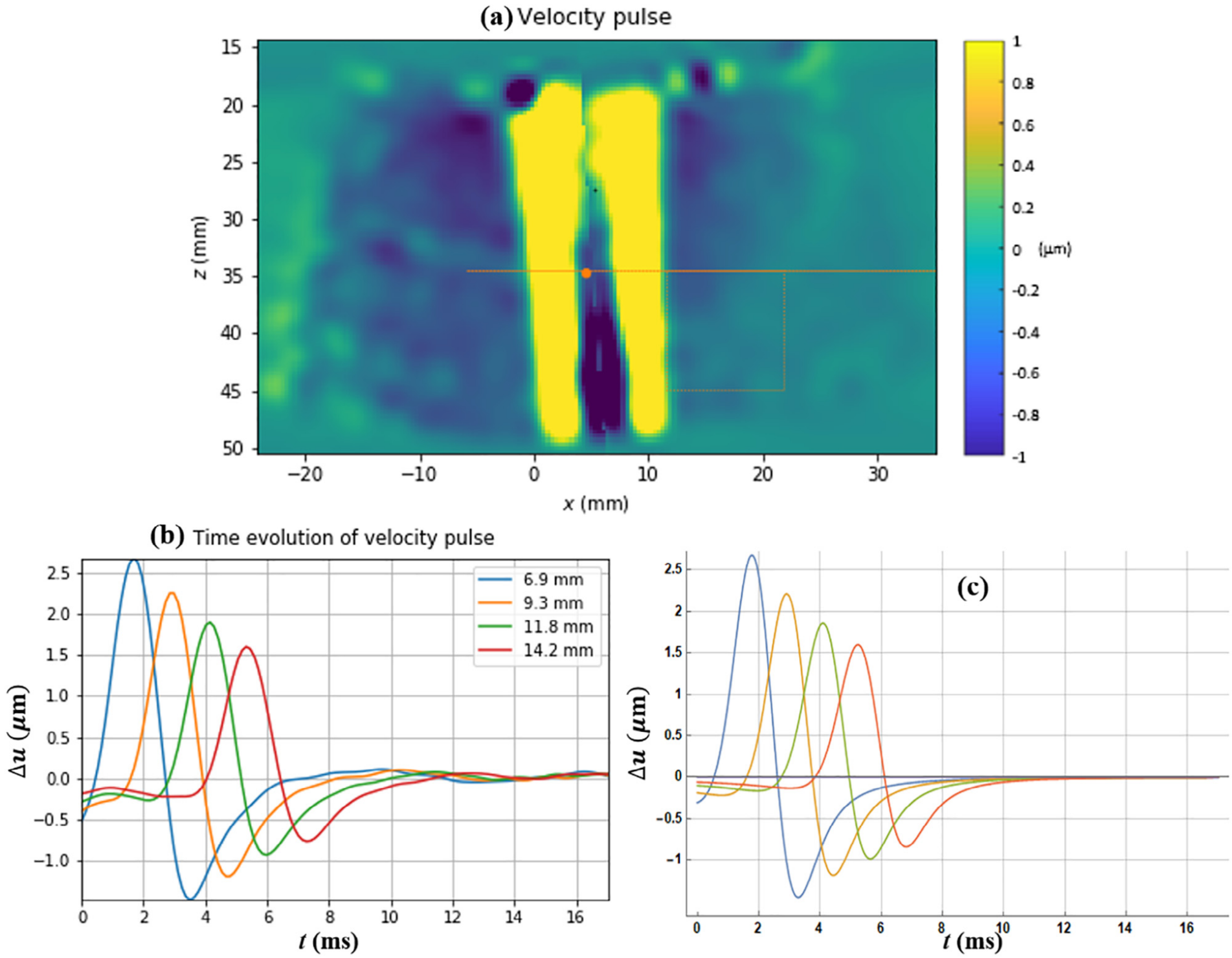

Fig. 2. (a) Snapshot of velocity values in two dimensions following a 0.65-ms push-pulse sequence in a CIRS breast phantom. (b) Shear wave propagation measured in the CIRS breast phantom at four locations. (c) Theoretical model using estimated parameters $R = 2$, $\sigma_x = 1.3$mm, $c = 2.12$ m/s and $\alpha = 0.067$ Np/mm/KHz. CIRS = Computerized Imaging Reference Systems, Norfolk, VA, USA.

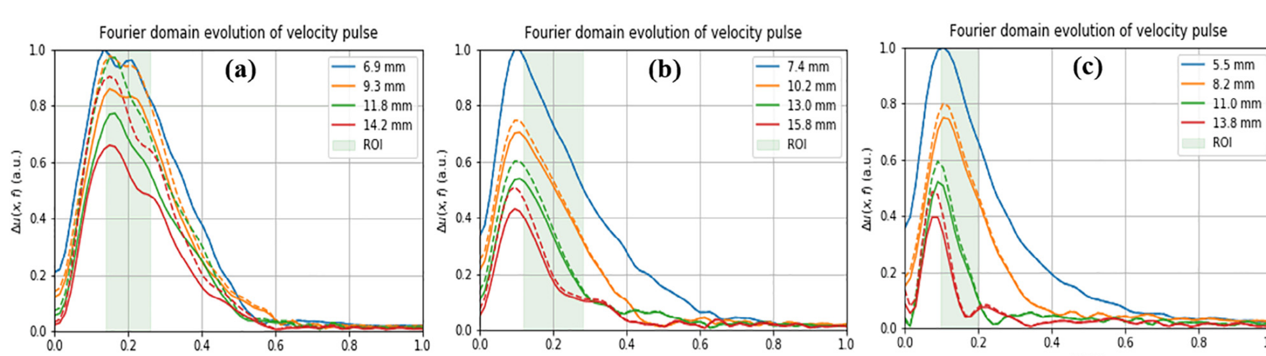

Fig. 3. Temporal Fourier transforms of shear wave measured in (a) the CIRS breast phantom, (b) the CIRS viscoelastic phantom and (c) *in vivo* human liver. The region of the frequency axis used for estimating α is shaded in *green*. The *solid lines* denote waveforms without correction for geometric spreading, and the *dashed lines* denote waveforms after correction for geometric spreading (see eqn [22]). CIRS = Computerized Imaging Reference Systems, Norfolk, VA, USA.

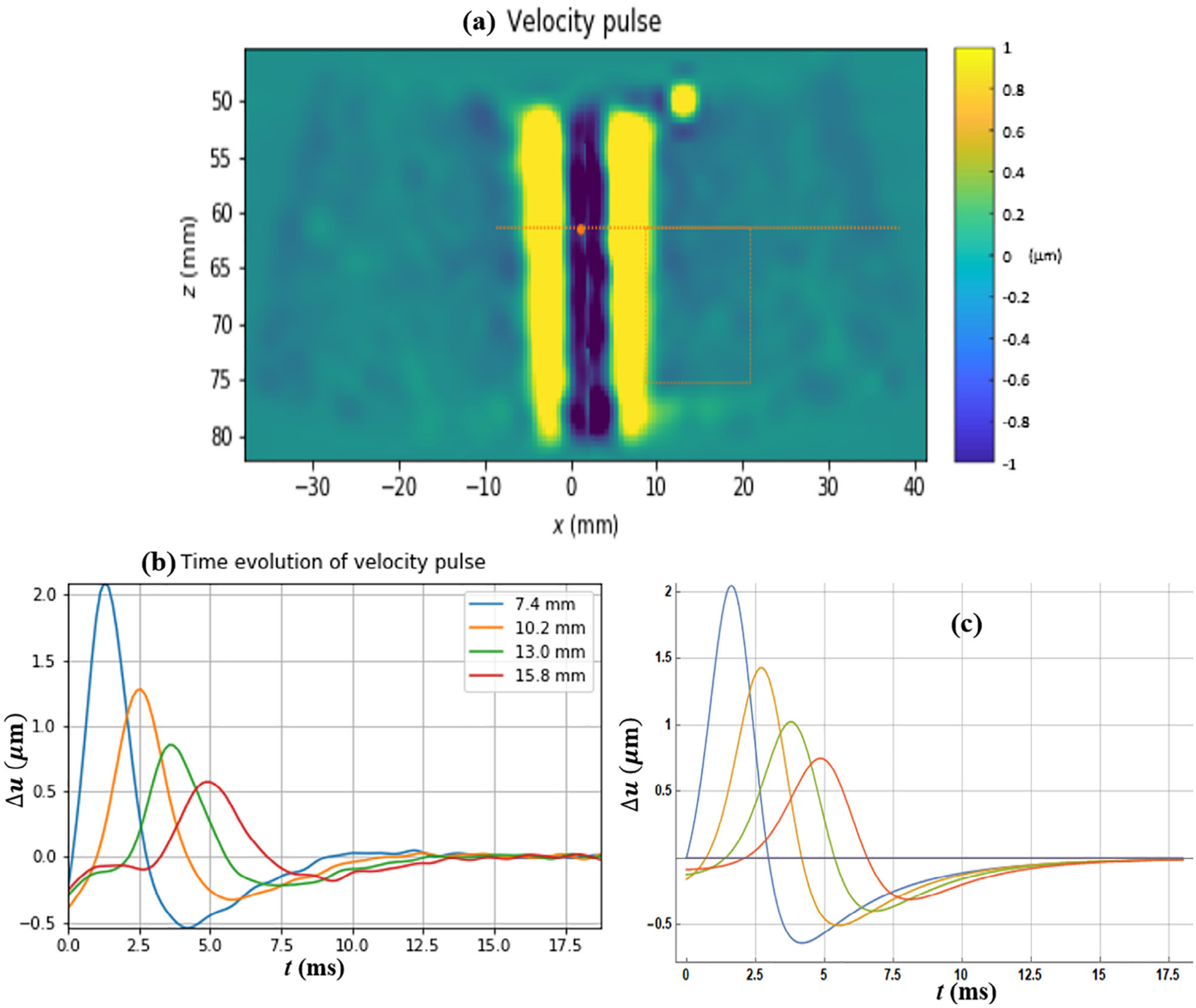

Fig. 4. (a) Snapshot of velocity values in two dimensions following a 0.65-ms push-pulse sequence in a CIRS viscoelastic phantom. (b) Shear wave propagation measured in the CIRS viscoelastic phantom at four locations. (c) Theoretical model using estimated parameters $R = 8$, $\sigma_x = 1.3$mm, $c = 2.46$ m/s and $\alpha = 0.667$ Np/mm/KHz. CIRS = Computerized Imaging Reference Systems, Norfolk, VA, USA; ROI = region of interest.

error) obtained from the experimental curves (Figs. 2b, 4b and 5b). In other phantom studies, we found that the kinetic energy group velocity estimator was more accurate than the least-squares error estimator using transformed phase relations. We attribute this in part to the imperfections of phase unwrapping, which can occur. Further corroboration is gained from independent measurements of phase velocity of shear waves within the CIRS breast and viscoelastic phantoms (Fig. 6a, 6b) and in the same normal human liver (Fig. 6c).

These measurements were obtained at discrete shear wave frequencies using the reverberant shear wave method described by Parker et al. (2017) and Ormachea et al. (2018). The breast and viscoelastic phantoms and the normal liver are seen to have a shear wave speed (SWS) group velocity of 2 m/s near 100 Hz, based on the estimations obtained from the models described in this article. These group velocities are higher than phase velocities measured using the reverberant shear wave methods at discrete frequencies. This is expected from the definitions of group velocity versus phase velocity in dispersive media (Blackstock 2000:ch. 9; Graff 1975). Furthermore, we note that the dispersion of SWS near 200 Hz using the reverberant shear wave method is in the range of 0.28 m/s per 100 Hz for the CIRS breast phantom, 0.59 m/s per 100 Hz for the CIRS viscoelastic phantom and 0.87 m/s per 100 Hz for the liver, consistent with other reports (see Barry et al. 2012; Deffieux et al. 2009; Muller et al. 2009; Parker et al. 2015), but lower than some magnetic resonance elastography estimates of dispersion (see Table 2 in Parker et al. 2015) obtained at

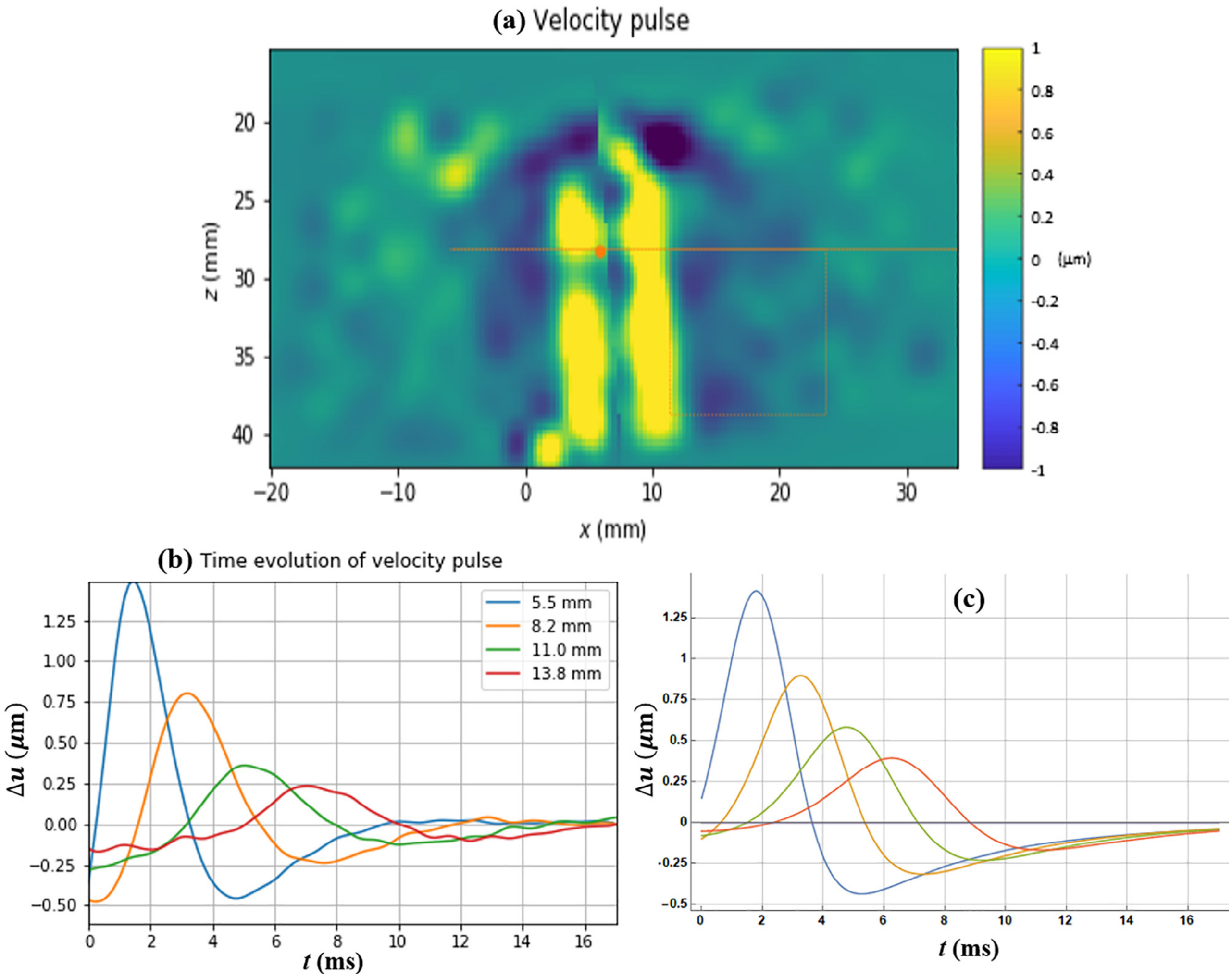

Fig. 5. (a) Snapshot of velocity values in two dimensions following a 0.65-ms push-pulse sequence in a normal human liver. (b) Shear wave propagation measured in the normal human liver at four locations. (c) Theoretical model using estimated parameters $R = 8$, $\sigma_x = 1.3$ mm, $c = 1.74$ m/s and $\alpha = 1.28$ Np/mm/KHz.

lower frequencies. Additional studies using an additional measurement, stress relaxation of isolated samples, are planned to further refine the expected value of the CIRS phantom's SWS and viscoelastic properties.

Some limitations of this study should be considered. The theory assumes that the push pulse is long in extent in the *z*-axis or depth and has an elevational focus that is broader by a factor of 2 or greater than the focus in the lateral plane. Thus, for low *f*-number, single focal depth and circularly symmetric transducers, the theory would not be expected to be accurate. In particular, the influence of low-intensity but extended regions above and below the focal region has been described by Bercoff et al. (2004b) using numerical methods. However, circularly symmetric solutions are found in Parker and Baddour (2014), and can be applied for higher *f*-number systems. Furthermore, the question of a gold-standard independent measurement of the viscoelastic properties of the liver and other soft tissues is longstanding. One complication is the known short-term fluctuations in SWS that are possible in the liver under a number of conditions (Cosgrove et al. 2013). The dynamic state of the vascular system in a soft tissue could be an influential co-factor in raising or lowering the SWS by measurable amounts over time (Parker 2014, 2015, 2017a, 2017b; Parker et al. 2016).

CONCLUSIONS

Analytical models were developed that can predict the shape of shear waves produced by push pulses in viscoelastic tissues. These closed-form solutions are also used to extract estimates of shear wave speed and shear wave attenuation, but do not rely on any single viscoelastic model for tissue and so do not depend on traditional Kelvin–

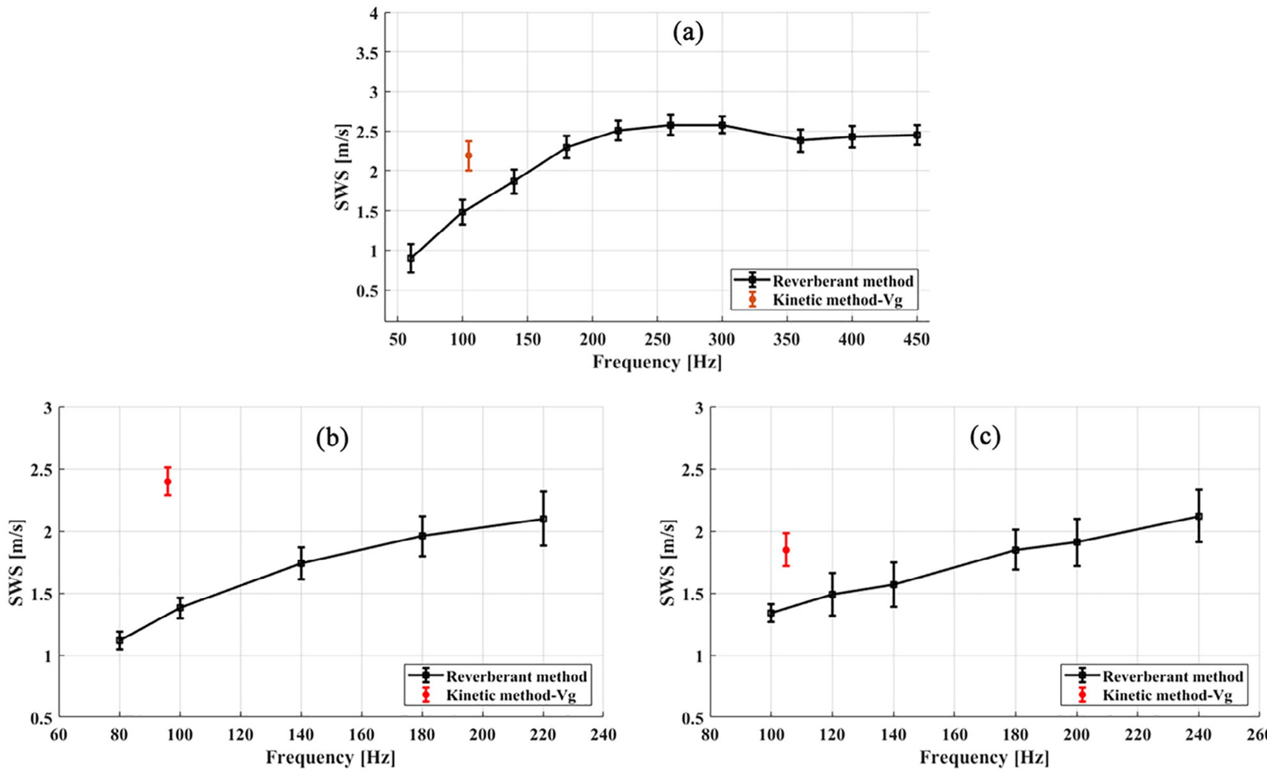

Fig. 6. Shear wave speed (phase velocity) measured in (a) the CIRS breast phantom, (b) the CIRS viscoelastic phantom, and (c) the normal human liver using kinetic energy moments estimate and reverberant field estimators at discrete frequencies. The corresponding group velocity frequencies were selected using the peak value from their temporal Fourier transforms signal. CIRS = Computerized Imaging Reference Systems, Norfolk, VA, USA; SWS = shear wave speed.

Voigt or Zener model parameters. By use of the forward propagation model and its estimators, good agreement was found between measured and predicted waveforms. Furthermore, the model and estimator results were properly bounded by independent measurements of a phantom and liver obtained from the reverberant shear wave method. These developments may be useful in quantifying the biomechanical state of soft tissues.

Acknowledgments—We are grateful for support from Samsung Medison and for the loan of equipment. Also, we thank Professor Natalie Baddour for insightful comments on the use of the integral theorems (Baddour 2011) that unlock many difficult equations in wave propagations.

REFERENCES

Abramowitz M, Stegun IA. Handbook of mathematical functions with formulas, graphs, and mathematical tables. Washington, DC: U.S. Govt. Printing Office; 1964.

Baddour N. Multidimensional wave field signal theory: Mathematical foundations. AIP Adv 2011;1:0221201.

Barry CT, Mills B, Hah Z, Mooney RA, Ryan CK, Rubens DJ, Parker KJ. Shear wave dispersion measures liver steatosis. Ultrasound Med Biol 2012;38:175–182.

Bercoff J, Tanter M, Fink M. Supersonic shear imaging: A new technique for soft tissue elasticity mapping. IEEE Trans Ultrason Ferroelectr Freq Control 2004a;51:396–409.

Bercoff J, Tanter M, Muller M, Fink M. The role of viscosity in the impulse diffraction field of elastic waves induced by the acoustic radiation force. IEEE Trans Ultrason Ferroelectr Freq Control 2004b;51:1523–1536.

Biot MA. General theorems on the equivalence of group velocity and energy transport. Phys Rev 1957;105:1129–1137.

Blackstock DT. Fundamentals of physical acoustics. New York: Wiley; 2000.

Bracewell RN. The Fourier transform and its applications. New York: McGraw-Hill; 1996. p. 248–249.

Broer LJF. On the propagation of energy in linear conservative waves. Appl Sci Res 1951;2:329.

Chen S, Fatemi M, Greenleaf JF. Quantifying elasticity and viscosity from measurement of shear wave speed dispersion. J Acoust Soc Am 2004;115:2781–2785.

Chen W, Holm S. Modified Szabo's wave equation models for lossy media obeying frequency power law. J Acoust Soc Am 2003;114:2570–2574.

Cosgrove D, Piscaglia F, Bamber J, Bojunga J, Correas JM, Gilja OH, Klauser AS, Sporea I, Calliada F, Cantisani V, D'Onofrio M, Drakonaki EE, Fink M, Friedrich-Rust M, Fromageau J, Havre RF, Jenssen C, Ohlinger R, Saftoiu A, Schaefer F, Dietrich CF EFSUMB. EFSUMB guidelines and recommendations on the clinical use of ultrasound elastography: Part 2. Clinical applications. Ultraschall Med 2013;34:238–253.

Deffieux T, Montaldo G, Tanter M, Fink M. Shear wave spectroscopy for in vivo quantification of human soft tissues visco-elasticity. IEEE Trans Med Imaging 2009;28:313–322.

Doyley MM. Model-based elastography: Survey of approaches to the inverse elasticity problem. Phys Med Biol 2012;57:R35–R73.

Fahey BJ, Nightingale KR, McAleavey SA, Palmeri ML, Wolf PD, Trahey GE. Acoustic radiation force impulse imaging of myocardial radiofrequency ablation: Initial in vivo results. IEEE Trans Ultrason Ferroelectr Freq Control 2005;52:631–641.
Fatemi M, Greenleaf JF. Ultrasound-stimulated vibro-acoustic spectrography. Science 1998;280:82–85.
Giannoula A, Cobbold RSC. Narrowband shear wave generation by a finite-amplitude radiation force: The fundamental component. IEEE Trans Ultrason Ferroelectr Freq Control 2008;55:343–358.
Giannoula A, Cobbold RSC. Propagation of shear waves generated by a modulated finite amplitude radiation force in a viscoelastic medium. IEEE Trans Ultrason Ferroelectr Freq Control 2009;56:575–588.
Graff KF. Wave motion in elastic solids. Oxford: Clarendon Press; 1975. p. 283–288.
Hah Z, Hazard C, Mills B, Barry C, Rubens D, Parker K. Integration of crawling waves in an ultrasound imaging system: Part 2. Signal processing and applications. Ultrasound Med Biol 2012;38:312–323.
Hazard C, Hah Z, Rubens D, Parker K. Integration of crawling waves in an ultrasound imaging system: Part 1. System and design considerations. Ultrasound Med Biol 2012;38:296–311.
Kazemirad S, Bernard S, Hybois S, Tang A, Cloutier G. Ultrasound shear wave viscoelastography: Model-independent quantification of the complex shear modulus. IEEE Trans Ultrason Ferroelectr Freq Control 2016;63:1399–1408.
Konofagou EE, Hynynen K. Localized harmonic motion imaging: Theory, simulations and experiments. Ultrasound Med Biol 2003;29:1405–1413.
Leartprapun N, Rishyashring I, Adie SG. Model-independent quantification of soft tissue viscoelasticity with dynamic optical coherence elastography. Proc SPIE 10053, Optical Coherence Tomography and Coherence Domain Optical Methods in Biomedicine XXI, 2017: 1005322.
McAleavey S, Menon M. 7B-3 Direct estimation of shear modulus using spatially modulated acoustic radiation force impulses. Proc IEEE Int Ultrason Symp 2007;558–561.
Muller M, Gennisson JL, Deffieux T, Tanter M, Fink M. Quantitative viscoelasticity mapping of human liver using supersonic shear imaging: Preliminary in vivo feasibility study. Ultrasound Med Biol 2009; 35:219–229.
Nenadic IZ, Qiang B, Urban MW, Zhao H, Sanchez W, Greenleaf JF, Chen S. Attenuation measuring ultrasound shearwave elastography and in vivo application in post-transplant liver patients. Phys Med Biol 2017;62:484–500.
Nightingale K, Nightingale R, Palmeri M, Trahey G. Finite element analysis of radiation force induced tissue motion with experimental validation. Proc IEEE Int Ultrason Symp 1999;2:1319–1323.
Ormachea J, Castaneda B, Parker KJ. Shear wave speed estimation using reverberant shear wave fields: Implementation and feasibility studies. Ultrasound Med Biol 2018;44:963–977.
Parker KJ. A microchannel flow model for soft tissue elasticity. Phys Med Biol 2014;59:4443–4457.
Parker KJ. Experimental evaluations of the microchannel flow model. Phys Med Biol 2015;60:4227–4242.
Parker KJ. Are rapid changes in brain elasticity possible? Phys Med Biol 2017a;62:7425–7439.
Parker KJ. The microchannel flow model under shear stress and higher frequencies. Phys Med Biol 2017b;62:N161–N167.
Parker KJ, Baddour N. The Gaussian shear wave in a dispersive medium. Ultrasound Med Biol 2014;40:675–684.
Parker KJ, Doyley MM, Rubens DJ. Imaging the elastic properties of tissue: The 20 year perspective. Phys Med Biol 2011;56:R1–R29.
Parker KJ, Partin A, Rubens DJ. What do we know about shear wave dispersion in normal and steatotic livers? Ultrasound Med Biol 2015; 41:1481–1487.
Parker KJ, Ormachea J, McAleavey SA, Wood RW, Carroll-Nellenback JJ, Miller RK. Shear wave dispersion behaviors of soft, vascularized tissues from the microchannel flow model. Phys Med Biol 2016; 61:4890–4903.
Parker KJ, Ormachea J, Zvietcovich F, Castaneda B. Reverberant shear wave fields and estimation of tissue properties. Phys Med Biol 2017; 62:1046.
Poularikas AD. Transforms and applications handbook. Boca Raton, FL: CRC Press; 2010.
Sarvazyan AP, Rudenko OV, Swanson SD, Fowlkes JB, Emelianov SY. Shear wave elasticity imaging: A new ultrasonic technology of medical diagnostics. Ultrasound Med Biol 1998;24:1419–1435.
Schmitt C, Hadj Henni A, Cloutier G. Ultrasound dynamic micro-elastography applied to the viscoelastic characterization of soft tissues and arterial walls. Ultrasound Med Biol 2010;36:1492–1503.
Szabo TL. Time domain wave equations for lossy media obeying a frequency power-law. J Acoust Soc Am 1994;96:491–500.
Urban MW, Chen SG, Greenleaf JF. Error in estimates of tissue material properties from shear wave dispersion ultrasound vibrometry. IEEE Trans Ultrason Ferroelectr Freq Control 2009;56:748–758.
Vappou J, Maleke C, Konofagou EE. Quantitative viscoelastic parameters measured by harmonic motion imaging. Phys Med Biol 2009; 54:3579–3594.
Wijesinghe P, McLaughlin RA, Sampson DD, Kennedy BF. Parametric imaging of viscoelasticity using optical coherence elastography. Phys Med Biol 2015;60:2293.
Zvietcovich F, Rolland JP, Parker KJ. An approach to viscoelastic characterization of dispersive media by inversion of a general wave propagation model. J Innov Opt Heal Sci 2017;10:1742008.

APPENDIX A

DERIVATION OF CONSTRAINED ESTIMATORS FOR *A* AND C_0

Suppose we have an estimation problem of the form

$$\mathbb{A} = c\mathbf{u}\mathbf{v}^T$$

where c is an unknown parameter and $\mathbb{A}$ is the system matrix. To obtain a least-squares estimator for c, we minimize the objective function

$$\begin{aligned} E(u, v, A) &= \sum_m \sum_n \left(A_{mn} - cu_m v_n\right)^2 \\ &= \sum_m \sum_n A_{mn}^2 - 2cA_{mn}u_m v_n + c^2 u_m^2 v_n^2 \end{aligned} \tag{44}$$

Compute the partial derivative $\partial_c E(u, v, A)$ with respect to the unknown parameter c and set to zero:

$$\partial_c E(u, v, A) = -2\sum_m \sum_n A_{mn}u_m v_n + 2c\sum_m \sum_n u_m^2 v_n^2 = 0 \tag{45}$$

Solving for c,

$$\begin{aligned} c &= \frac{\sum_m \sum_n A_{mn} u_m v_n}{\sum_m \sum_n u_m^2 v_n^2} \\ &= \frac{\sum_m u_m \sum_n A_{mn} v_n}{\sum_m u_m^2 \sum_n v_n^2} \\ &= \frac{\mathbf{u}^T \mathbb{A} \mathbf{v}}{\left(\mathbf{u}^T\mathbf{u}\right)\left(\mathbf{v}^T\mathbf{v}\right)} \end{aligned} \tag{46}$$

APPENDIX B

DERIVATION OF UNCONSTRAINED ESTIMATORS FOR A AND C_0

Here, we model the surface of best fit as a general second-order surface in x and y of the form

$$f(u, v) = a_0 + a_1 u + a_2 v + a_3 uv + a_4 u^2 + a_5 v^2 \tag{47}$$

and accordingly minimize the objective function

$$E(u, v, A) = \sum_m \sum_n \left(A_{mn} - f(u_m, v_n)\right)^2 \tag{48}$$

Differentiating with respect to each of the six unknown parameters and setting each equation to zero, we obtain a system of normal equations, written below in matrix form, using the shorthand notation $u_p \equiv \|\mathbf{u}\|_p^p$ (*i.e.*, the ℓ_p norm of the vector $\mathbf{u}$ raised to the pth power) and $\mathbf{u} \otimes \mathbf{u}$ to denote elementwise multiplication:

$$\begin{bmatrix} 1_1 & u_1 & v_1 & u_1 v_1 & u_2 & v_2 \\ u & u_2 & u_1 v_1 & u_2 v_1 & u_3 & u_1 v_2 \\ v_1 & u_1 v_1 & v_2 & u_1 v_2 & u_2 v_1 & v_3 \\ u_1 v_1 & u_2 v_1 & u_1 v_2 & u_2 v_2 & u_3 v_1 & u_1 v_3 \\ u_2 & u_3 & u_2 v_1 & u_3 v_1 & u_4 & u_2 v_2 \\ v_2 & u_1 v_2 & v_3 & u_1 v_3 & u_2 v_2 & v_4 \end{bmatrix} \begin{bmatrix} a_0 \\ a_1 \\ a_2 \\ a_3 \\ a_4 \\ a_5 \end{bmatrix} = \begin{bmatrix} \mathbf{1}^T \mathbb{A} \mathbf{1} \\ \mathbf{u}^T \mathbb{A} \mathbf{1} \\ \mathbf{1}^T \mathbb{A} \mathbf{v} \\ \mathbf{u}^T \mathbb{A} \mathbf{v} \\ (\mathbf{u} \otimes \mathbf{u})^T \mathbb{A} \mathbf{v} \\ \mathbf{u}^T \mathbb{A} (\mathbf{v} \otimes \mathbf{v}) \end{bmatrix} \tag{49}$$

Also note that $\mathbf{1}$ refers to the vector whose elements are all unity, and whose dimension changes in the context of its use. The vector $\mathbf{1}$ in the upper left-hand corner of the matrix in eqn (49) has MN elements, where M and N are the dimensions of $\mathbf{u}$ and $\mathbf{v}$, respectively, while the vector $\mathbf{1}$ on the right-hand side of the equation is either M- or N-dimensional depending on whether it is used in a right-hand or left-hand multiplication with $\mathbb{A} \in \mathbb{R}^{M \times N}$.